Supporting Information for

Redispersion Mechanisms of 2D Nanosheets: Combined Role of Intersheet Contact and Surface Chemistry

Bei Liu[a#], Jingyan Zhang[b,c#], Qi Han[a], Yufei Shu[a], Li Wang[a], Hui Li[c], Lei Li[b*], Zhongying Wang[a*]

[a] School of Environmental Science and Engineering
Southern University of Science and Technology
Shenzhen 518055, China
[b] Department of Material Science and Engineering
Southern University of Science and Technology
Shenzhen 518055, China
[c] Beijing Advanced Innovation Center for Soft Matter Science and Engineering
Beijing University of Chemical Technology
Beijing 100029, China

[*] The author to whom correspondence should be addressed. e-mail: wangzy6@sustech.edu.cn; lil33@sustech.edu.cn; [#] These authors contributed equally to this work.

Table of content

1. Supplementary Experimental Section

Evaluation of Hamaker Constants. To evaluate the vdW forces between nanosheets of pristine and transformed GO and MoS_2, the Hamaker constants in water were evaluated. Based on the Lifshitz theory for dispersion forces, the Hamaker constant between two semi-infinite media across a medium (water) can be estimated as follows:

$$H_{total} \approx \frac{3hv_e}{8\sqrt{2}} \times \frac{(n_1^2 - n_3^2)(n_2^2 - n_3^2)}{\sqrt{n_1^2 + n_3^2} \times \sqrt{n_2^2 + n_3^2} \times (\sqrt{n_1^2 + n_3^2} + \sqrt{n_2^2 + n_3^2})}$$

where $n_1 = n_2 = n$ is the refractive index of interacting nanosheets in visible regime, n_3 is the refractive index of water (1.33), h is the Planck constant (6.626×10^{-34} Js), and v_e is the main absorption frequency in the UV region, which could be obtained through the following equation:

$$v_e = v_I\sqrt{3/(n^2 + 2)}$$

where v_I is the absorption frequency of a Bohr atom (3.3×10^{15} s^{-1}).

To the best of our knowledge, there's no data available for the refractive index n of GO, MoS_2 nanosheets and transformed ones. However, it was reported the average n of GO and rGO in visible regime are around 1.85 and 2.6, respectively;[1,2] and the average n of monolayer 1T MoS_2 and 2H MoS_2 are around 2.5 and 4.0, respectively.[3,4] Therefore, the H for GO and rGO in water is thus between 49 and 260×10^{-21} J, and H of 1T-MoS_2 and 2H-MoS_2 is between 154 and 320×10^{-21} J. A linear increase of H was assumed during reduction of GO and phase transformation of MoS_2.

First-principles calculations. First-principles calculations were performed in the framework of the density functional theory (DFT) method as implemented in the Vienna Ab Initio Simulation Package (VASP).[5,6] The project-augmented-wave (PAW) method[7,8] with plane wave basis sets were employed to treat the core-electron interaction. The generalized gradient approximation (GGA) in the Perdew-Burke-Ernzerhof (PBE)[9] form was applied to describe the exchange and correlation energy.

The energy cutoff was 400 eV. The Monkhorst-Pack scheme with a 1 × 1 × 1 k-point grid was adopted to sample the Brillouin zone.[10] All the atomic structures were relaxed until the force was below 0.05 eV/Å. A model consisting of two 35×39 $Å^2$ MoS_2 nanoribbons with a tilt angle was used to model the variation of the system energy with the interlayer distance (see Figure S16d). A ~15 Å vacuum layer was used to avoid interaction from neighboring cells in both the *x* and *z* directions.

2. Supplementary Results

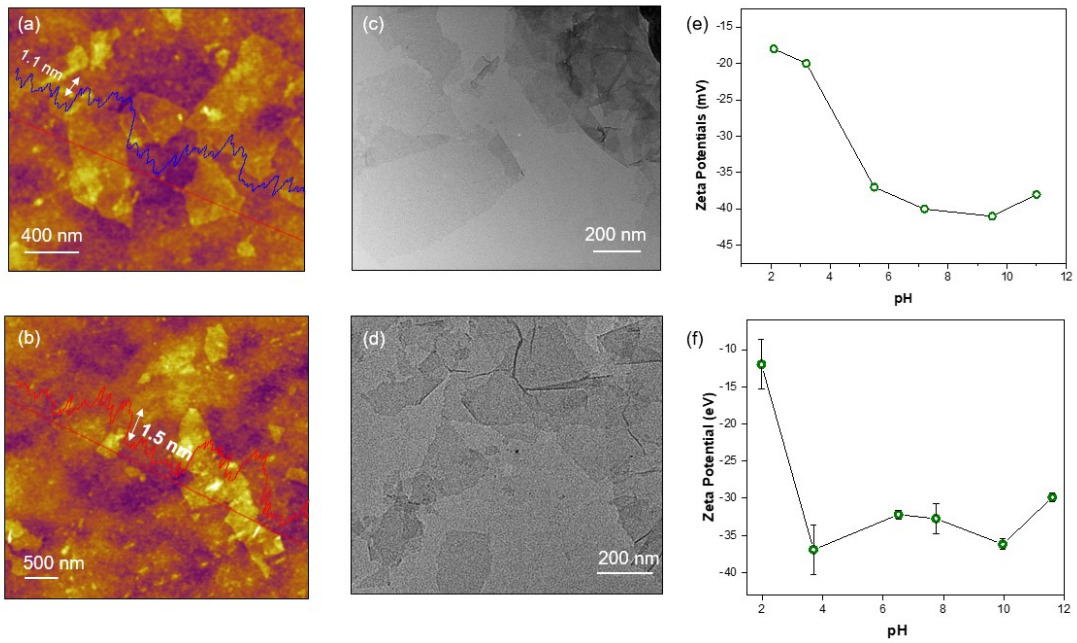

Figure S1. Characterization of MoS_2 (a, c, e) and GO (b, d, f) nanosheets: (a-b) representative AFM image, inset: line scan showing the thickness profile along the red line in the image; (c-d) representative TEM image; (e-f) apparent ζ potentials as a function of pH.

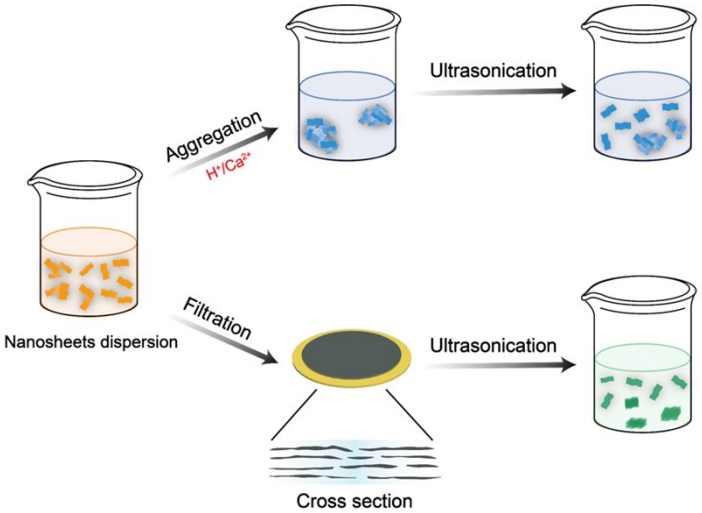

Figure S2. Schematic illustration for the creation and the redispersion of random aggregates and aligned stacks.

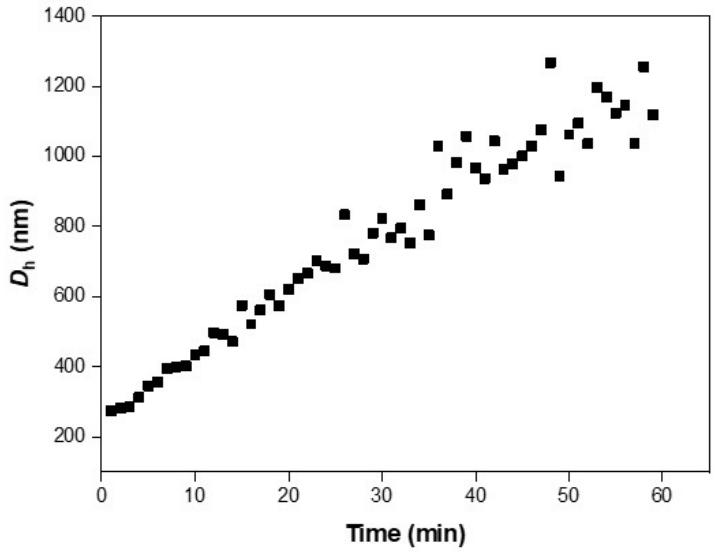

Figure S3. Rising hydrodynamic diameter of MoS_2 dispersion at pH 3. The results suggested that a low pH could induce the aggregation of the nanosheets and thus destroy the colloidal stability by providing adequate H^+.

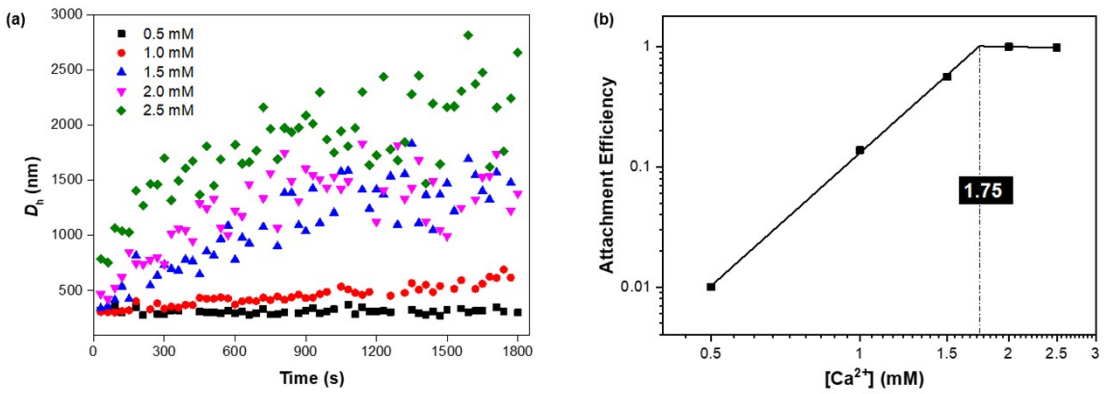

Figure S4. Aggregation of GO dispersion: (a) evolution of hydrodynamic diameter of GO in the solutions containing a series of concentrations of Ca^{2+}; (b) attachment efficiency as a function of Ca^{2+} concentrations, from which the critical coagulation concentration (CCC) of 1.75 mM was obtained. Therefore, a concentration of 2 mM Ca^{2+} was employed in the study to induce the nanosheets aggregation, which is higher than CCCs of Ca^{2+} for GO (1.75 mM) and MoS_2 (0.9 mM).[11]

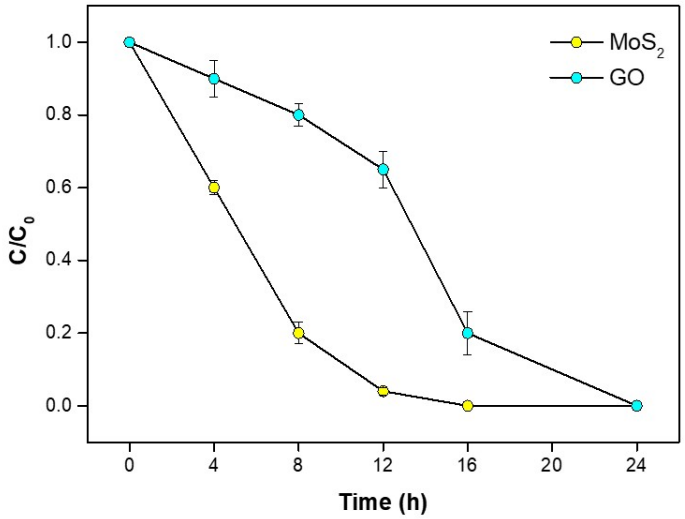

Figure S5. Evolution of the normalized suspended concentration of MoS_2 and GO in the solution containing 2 mM Ca^{2+}.

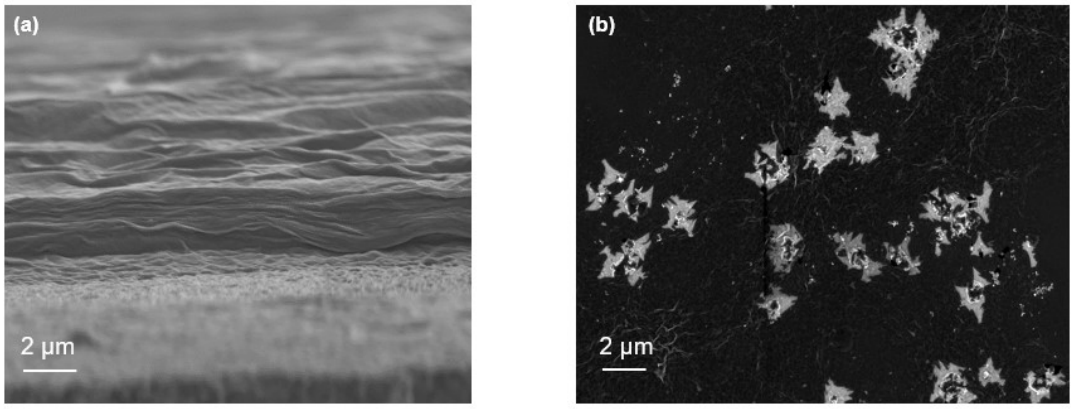

Figure S6. SEM characterization of aligned stacks and aggregates of GO: (a) cross-section image of GO stacks obtained by filtration and (b) top view of GO aggregates.

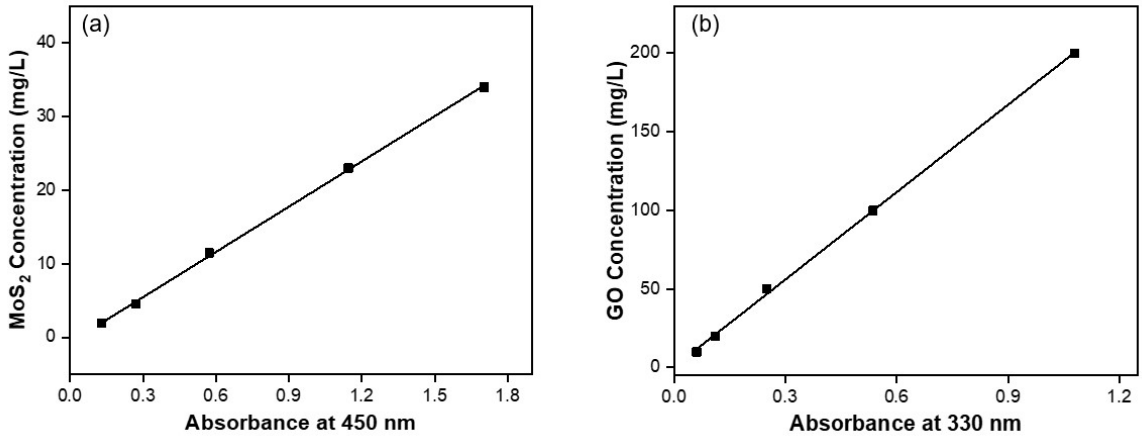

Figure S7. Linear correlation of the absorbance to the concentration of nanosheets dispersion: (a) SL-MoS_2 at 450 nm and (b) GO at 330 nm.

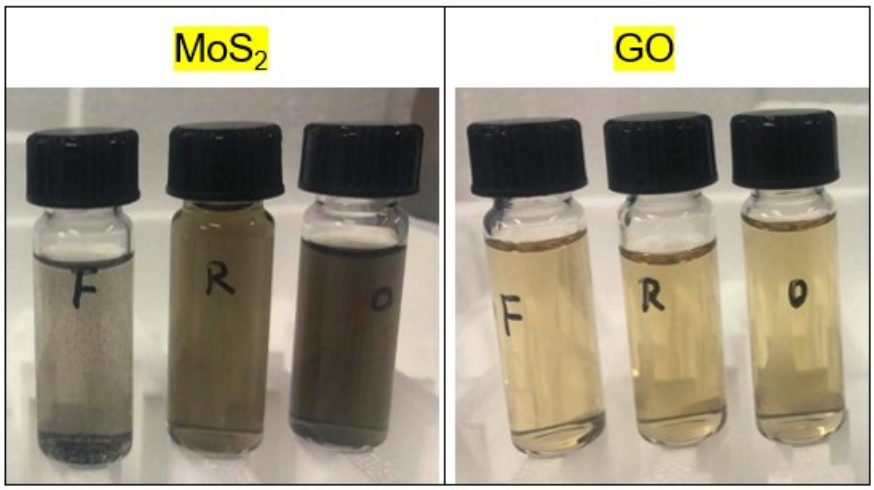

Figure S8. Photographs of the original dispersion and redispersion obtained from the random aggregates and aligned stacks. Left: MoS_2; right: GO (F: redispersion of stacks created by filtration; R: redispersion from random aggregates; O: original dispersion).

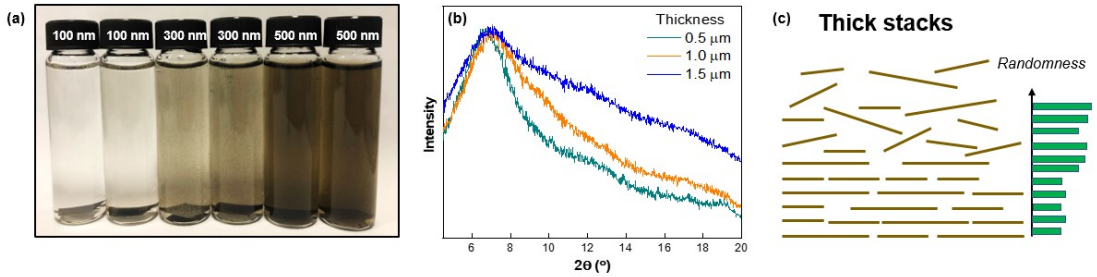

Figure S9. Redispersion from MoS_2 stacks as a function of thickness: (a) images of redispersion, with redispersion efficiency of 1%, 29% and 54% from the stacks with thickness of 100, 300 and 500 nm, respectively; (b) XRD patterns, showing a broadening peak as the increase of thickness; (c) schematic illustration of randomness as influenced by the thickness of MoS_2 stacks.

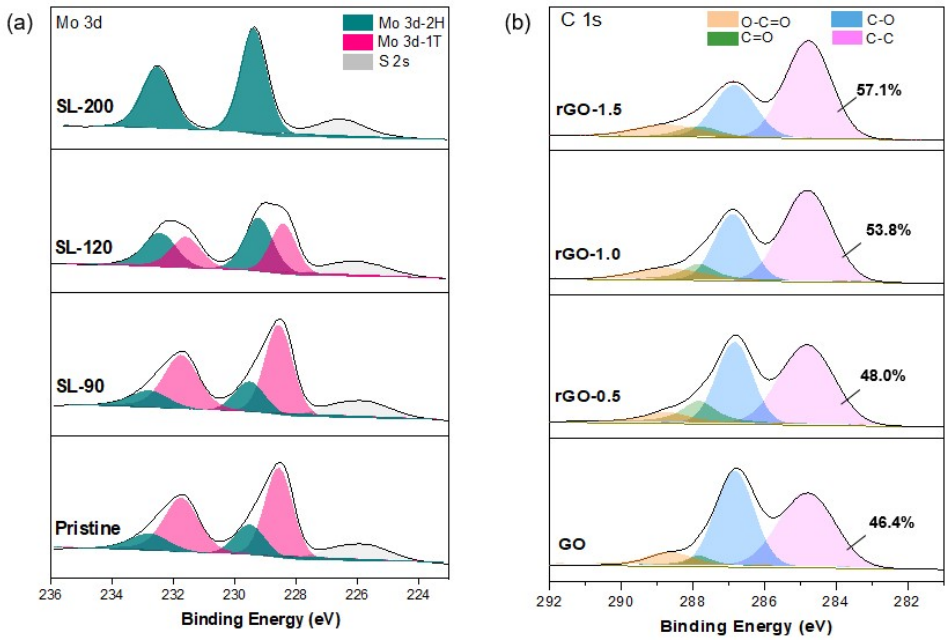

Figure S10. XPS characterizations on the composition deconvolution of MoS_2 and GO during transformation: (a) Mo 3d of MoS_2 nanosheets, showing the increasing fraction of 2H phase during hydrothermal treatment, and (b) C 1s of GO during the reduction reaction, suggesting the restoration of C–C/C=C during reaction.

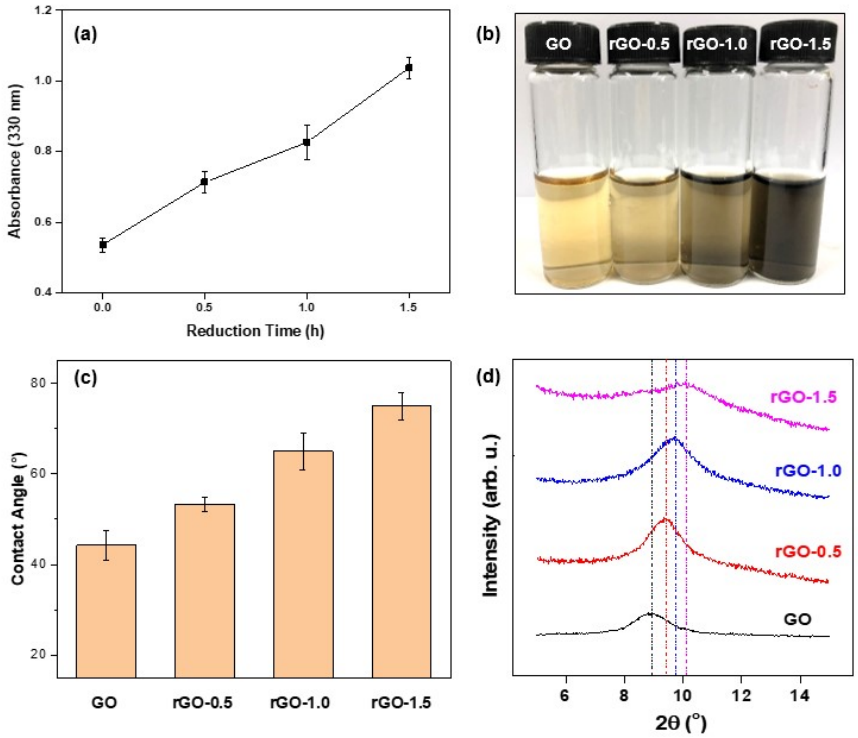

Figure S11. Characterization of GO and rGO obtained through chemical reduction: (a) absorbance at 330 nm in the concentration of 100 mg/L; (b) photograph of the dispersion (100 mg/L); (c) water contact angles and (d) XRD patterns of restacked GO and rGO.

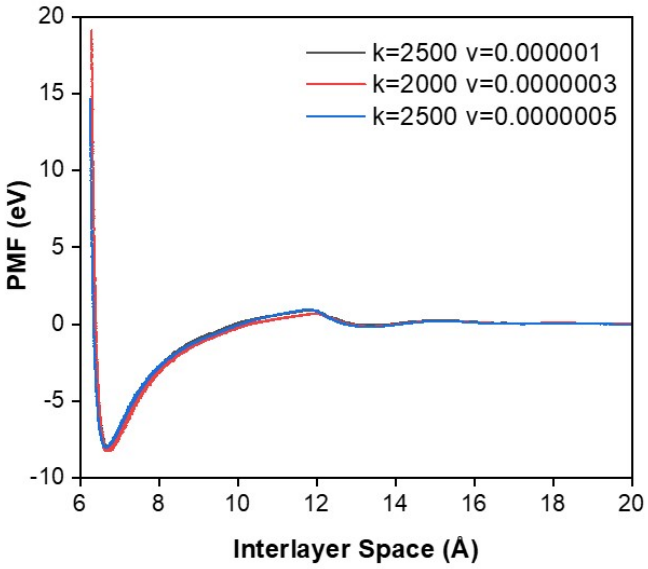

Figure S12. SMD simulation results of system at k_{spring} = 2500 kcal/mol/Å^2 with various pulling speed from 0.0000005 to 0.000001 Å/fs.

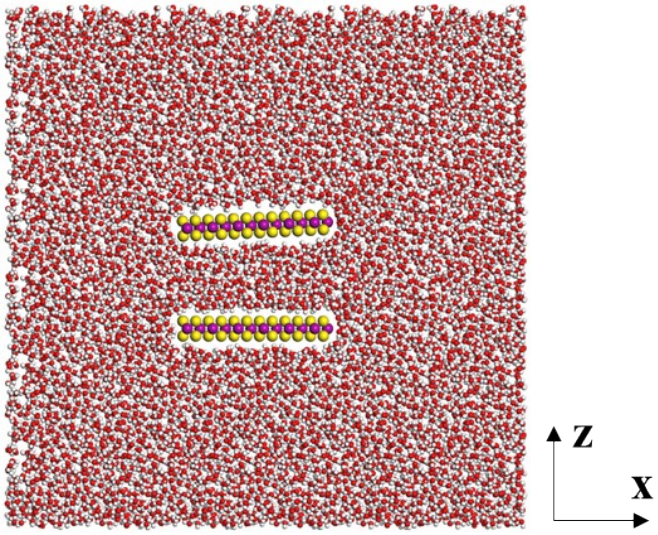

Figure S13. Snapshot of an MD simulation used to compute the PMFs showing the full extent of the simulation box in the x- and z-directions.

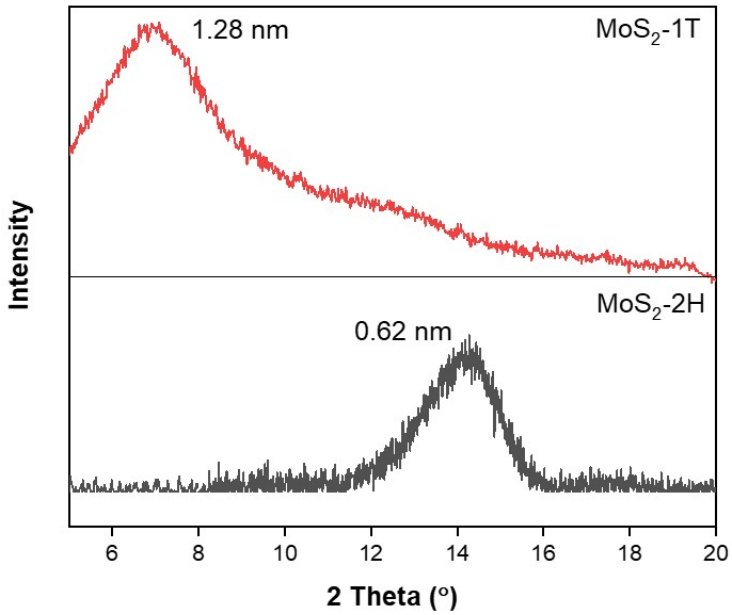

Figure S14. XRD patterns of as-created (wet) MoS_2 stacks from SL-pristine dominant in 1T phase and SL-200 in pure 2H phase, with the interlayer spacing of 1.28 and 0.62 nm identified, respectively.

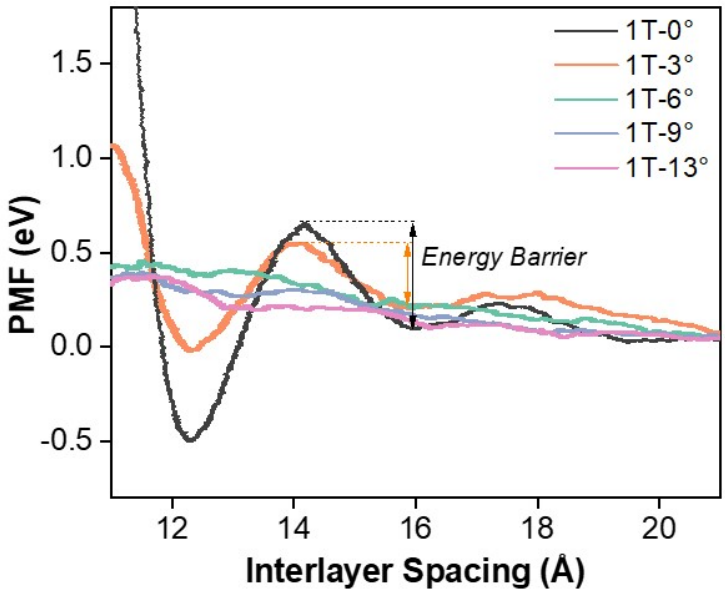

Figure S15. PMF as a function of interlayer spacing for 1T phase of MoS_2 with various tilt angles. The simulated models are built with S atoms being exposed outside.

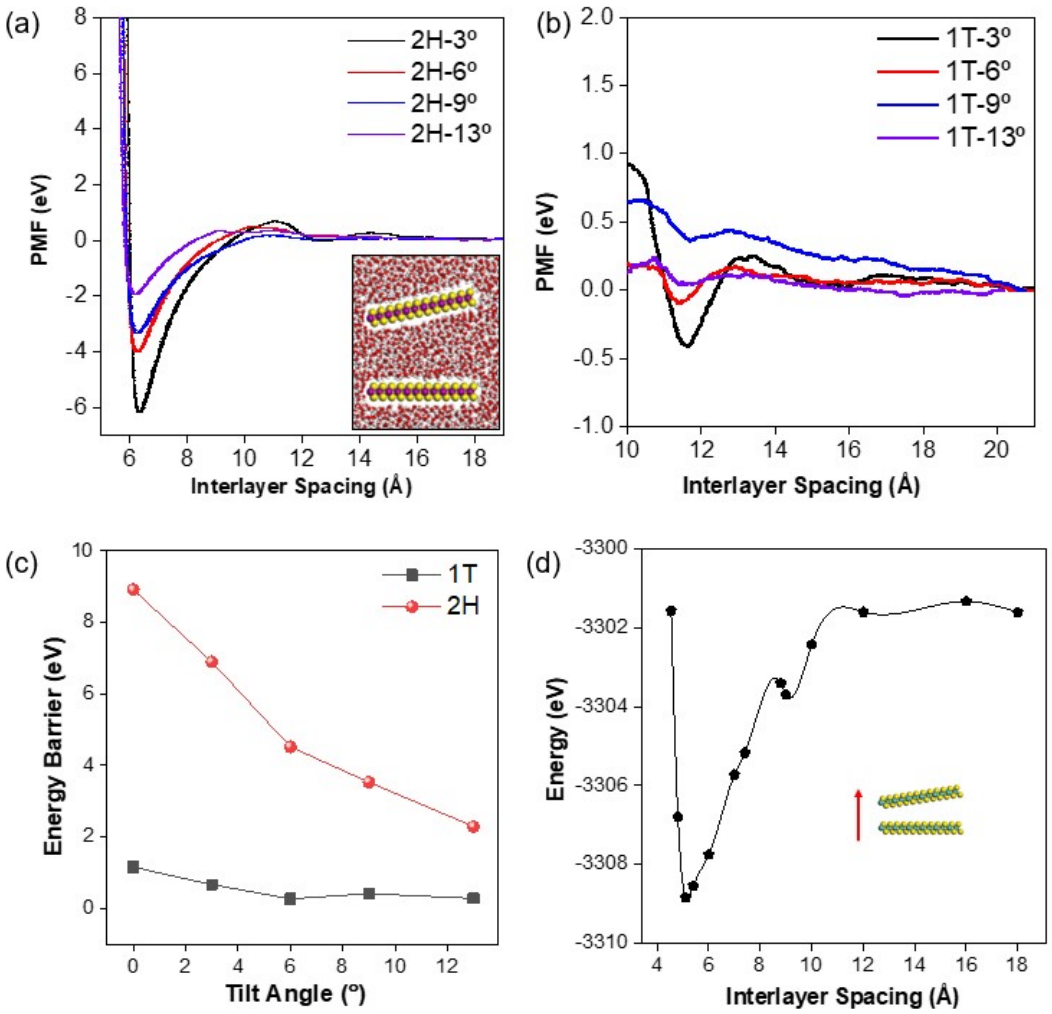

Figure S16. PMF calculations for 1T and 2H MoS_2 tilted at the Mo end: (a-b) the PMF profiles of 2H (a) and 1T (b) MoS_2 at various tilt angles (inset: the schematic illustration of the tilt model of two MoS_2 layers in water solution); (c) the redispersion barrier of 1T and 2H MoS_2 changes with the tilt angle; and (d) the total energy of the tilted 1T MoS_2 in vacuum (tilt angle=9°) changes with interlayer spacing based on first-principles calculations.

Table S1 Water contact angle and Hamaker constant of nanosheets

Nanosheets	Hamaker constant ($\times 10^{-21}$ J)	Water contact angle (˚)
GO	49	45
rGO-0.5	62	53.3
rGO-1.0	108	69
rGO-1.5	135	88
MoS_2	154	58
MoS_2-90	159	60
MoS_2-120	218	72
MoS_2-200	320	98
WS_2	320[12]	78[13]
h-BN	764[12]	81[14]
MXene	48.7[15]	24.8[16]
AlMg-LDH	14[17]	21.4[18]

References

1 M. M. Gudarzi, *Langmuir*, 2016, **32**, 5058–5068.

2 I. Jung, M. Vaupel, M. Pelton, R. Pinery, D. A. Dikin, S. Stankovich, J. An and R. S. Ruoff, *J. Phys. Chem. C*, 2008, **112**, 8499–8506.

3 X. Yin, C. S. Tang, D. Wu, W. Kong, C. Li, Q. Wang, L. Cao, M. Yang, Y. H. Chang, D. Qi, F. Ouyang, S. J. Pennycook, Y. P. Feng, M. B. H. Breese, S. J. Wang, W. Zhang, A. Rusydi and A. T. S. Wee, *Adv. Sci.*, , DOI:10.1002/advs.201802093.

4 H. Zhang, Y. Ma, Y. Wan, X. Rong, Z. Xie, W. Wang and L. Dai, *Sci. Rep.*, 2015, **5**, 1–7.

5 G. Kresse and J. Furthmüller, *Comput. Mater. Sci.*, 1996, **6**, 15–50.

6 G. Kresse and J. Furthmüller, *Phys. Rev. B - Condens. Matter Mater. Phys.*, 1996, **54**, 11169–11186.

7 P. E. Blöchl, *Phys. Rev. B*, 1994, **50**, 17953–17979.

8 G. Kresse and D. Joubert, *Phys. Rev. B - Condens. Matter Mater. Phys.*, 1999, **59**, 1758–1775.

9 J. P. Perdew, K. Burke and M. Ernzerhof, *Phys. Rev. Lett.*, 1996, **77**, 3865–3868.

10 H. J. Monkhorst and J. D. Pack, *Phys. Rev. B*, 1976, **13**, 5188–5192.

11 B. Liu, Q. Han, L. Li, S. Zheng, Y. Shu, J. A. Pedersen and Z. Wang, *Environ. Sci. Technol.*, 2021, **55**, 16379–16389.

12 T. M. Mohona, A. Gupta, A. Masud, S. C. Chien, L. C. Lin, P. C. Nalam and N. Aich, *Environ. Sci. Technol.*, 2019, **53**, 4161–4172.

13 P. K. Chow, E. Singh, B. C. Viana, J. Gao, J. Luo, J. Li, Z. Lin, A. L. Elías, Y. Shi, Z. Wang, M. Terrones and N. Koratkar, *ACS Nano*, 2015, **9**, 3023–3031.

14 A. Govind Rajan, M. S. Strano and D. Blankschtein, *Nano Lett.*, 2019, **19**, 1539–1551.

15 J. Lao, R. Lv, J. Gao, A. Wang, J. Wu and J. Luo, *ACS Nano*, 2018, **12**, 12464–12471.

16 S. Shen, T. Ke, K. Rajavel, K. Yang and D. Lin, *Small*, 2020, **16**, 2002433.

17 D. Takács, B. Katana, A. Szerlauth, D. Sebők, M. Tomšič and I. Szilágyi, *Soft Matter*, 2021, **17**, 9116–9124.

18 X. Han, J. Hu, Y. Q. Wang, T. B. Xiao, W. Xia, Y. N. Chen and L. Wu, *Front. Mater.*, 2021, **8**, 1–12.